REPORT DOCUMENTATION PAGE

Form Approved
OMB NO. 0704-0188

1. AGENCY USE ONLY (Leave Blank)	2. REPORT DATE November 18, 2004	3. REPORT TYPE AND DATES COVERED Final; May 17, 2004 – November 16, 2004

4. TITLE AND SUBTITLE
Novel THz-frequency Spectrometers by Integrating Widely-Tunable Monochromatic THz Sources and Detectors, or Arrays of Emitters and Detectors, With Photonic Bandgap Crystals

5. FUNDING NUMBERS
W911NF-04-C-1235

6. AUTHOR(S)
Yuliya Zotova

7. PERFORMING ORGANIZATION NAME(S) AND ADDRESS(ES)
ArkLight
P. O. Box 2
Center Valley, PA 18034

8. PERFORMING ORGANIZATION REPORT NUMBER ARK0006z

9. SPONSORING / MONITORING AGENCY NAME(S) AND ADDRESS(ES)
U. S. Army Research Office
P.O. Box 12211
Research Triangle Park, NC 27709-2211

10. SPONSORING / MONITORING AGENCY REPORT NUMBER
47024.1-EL-CBD

11. SUPPLEMENTARY NOTES
The views, opinions and/or findings contained in this report are those of the author(s) and should not be construed as an official Department of the Army position, policy or decision, unless so designated by other documentation.

12 a. DISTRIBUTION / AVAILABILITY STATEMENT	12 b. DISTRIBUTION CODE
Approved for public release; distribution unlimited.	

13. ABSTRACT (Maximum 200 words)

We have successfully carried out our Phase-I research by achieving most of the Phase-I objectives. First, we have significantly extended the tuning range of our THz source and increased the output peak powers. Second, we have used our tunable THz source to measure the absorption spectra of several chemicals in the vapor phase, and therefore, we have demonstrated the feasibility of fingerprinting molecules. Third, we have used our tunable THz source to take a THz picture of an object (proof of principle). Fourth, we have observed up-conversion process, which can be used as a new detection scheme for THz waves at room temperature. Finally, we have systematically investigated unique THz properties of photonic crystals.

14. SUBJECT TERMS	15. NUMBER OF PAGES
Photonic crystals Tunable THz waves THz Spectrometers Difference-frequency generation	9 16. PRICE CODE

17. SECURITY CLASSIFICATION OR REPORT	18. SECURITY CLASSIFICATION ON THIS PAGE	19. SECURITY CLASSIFICATION OF ABSTRACT	20. LIMITATION OF ABSTRACT
UNCLASSIFIED	**UNCLASSIFIED**	**UNCLASSIFIED**	**UL**

Final Monthly Report

November 16, 2004

W911NF-04-C-1235

Period of Performance May 17, 2004 – November 16, 2004

"Novel THz-frequency Spectrometers by Integrating Widely-Tunable Monochromatic THz Sources and Detectors, or Arrays of Emitters and Detectors, With Photonic Bandgap Crystals"

Purchase Request Number: R-47024-EL-CBD-01110-1

Project: 47024-EL-CBD

CLIN 0001AE

Yuliya B. Zotova

ArkLight

P. O. Box 2

Center Valley, PA 18034

Since May 17, 2004, we have successfully completed our Phase-I research by achieving most of the Phase-I objectives. Below, we have summarized our results obtained from the Phase-I work.

Further development of THz source

In order to find out the ultimate sensitivity for our THz spectrometer, we have further improved our THz source. Indeed, based on a backward configuration, we have extended our tuning range achieved previously to that from 167.6 μm to 2060 μm, see Fig. 1. The peak power reaches 208 W at 207 μm. The backward configuration has an advantage over the forward one. Since the THz wave propagates in the direction opposite to that for the pump waves, it is much easier for us to separate the THz wave from the pump beams. This feature is quite important for our on-going up-conversion experiment.

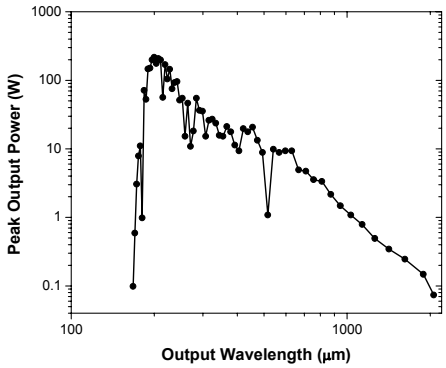

Fig. 1. Peak power vs. output wavelength for backward difference-frequency generation.

Chemical sensing

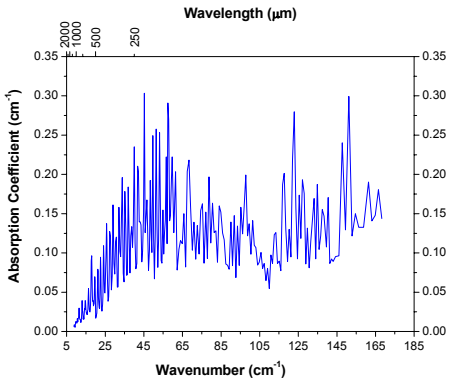

Fig. 2. Absorption coefficient is measured vs. wavenumber for the methanol vapor.

To test our THz absorption spectrometer, we have assembled our THz source and bolometer together to directly measure the absorption spectra of gaseous chemicals. In order to measure the transmittance for each type of the chemicals in the vapor phase, we have used the two identical gas cells both of which are 15 cm long. One cell is filled by a small amount of the high-purity chemical in the liquid form at the temperature of 23°C and pressure of 1 atm. Another cell is filled by high-purity helium gas at the same temperature and pressure, which is used as a reference. By frequency-tuning a coherent and monochromatic THz source, we have

measured the transmittances for the THz wave going through each kind of the chemicals in the vapor phase. We can then determine the absorption coefficient as a function of the frequency.

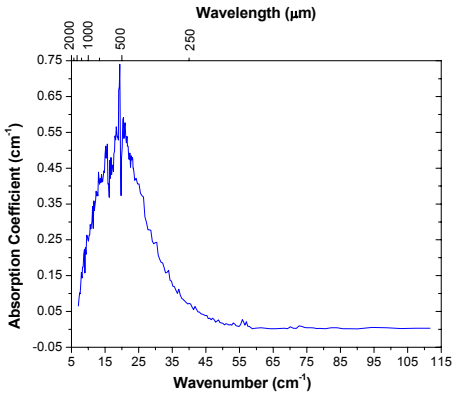

Fig. 3. Absorption coefficient is measured vs. wavenumber for the acetone vapor.

By frequency-tuning our THz sources we have directly measured the absorption spectra for methanol vapor (CH_3OH, Fig. 2), ethanol vapor (C_2H_5OH), isopropanol vapor (C_3H_7OH), acetone vapor [$(CH_3)_2CO$, Fig. 3], the vapor of methyl ethyl ketone (C_3H_8CO), dichloromethane vapor (CH_2Cl_2, Fig. 4), and chloroform vapor ($CHCl_3$). *All these vapors exhibit completely different sets of the transition peaks. In particular, the spectra for the three types of the alcohols (methanol, ethanol, and isopropanol), having similar molecular structures, are very different. On the other hand, the spectra for the two types of the solvents (acetone and methyl ethyl ketone), having similar molecular structures, are also different. Among all these chemicals,* dichloromethane vapor (CH_2Cl_2) exhibits 29 sharp transition peaks in the range of 5-60 cm^{-1}, see Fig. 4. *These are evenly-spaced transitions in frequency*, indicating that there are no contributions to the transitions due to the torsional motion, i.e. *the transitions only occur between two rotational energy states*. According to our measurements, the spacing between the adjacent transition energies is about 1.84 cm^{-1}. *These are very important findings of ours. They can be regarded as the basis for the proposed THz spectrometers.*

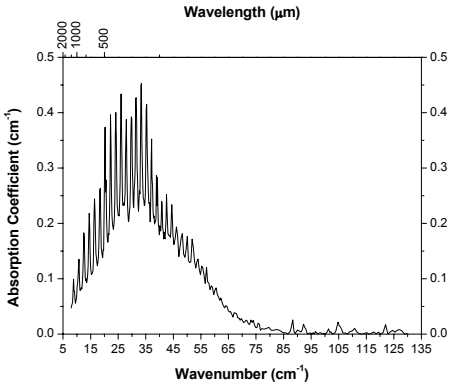

Fig. 4. Absorption coefficient is measured vs. wavenumber for dichloromethane vapor.

THz imaging

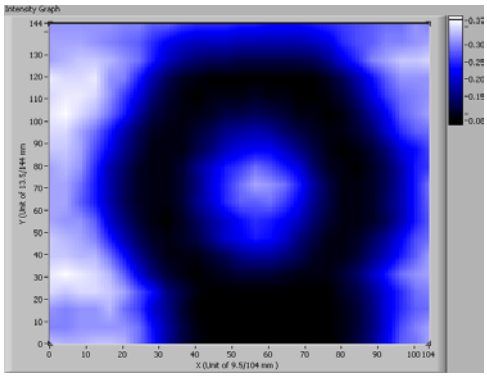

Fig. 5. Spatial distribution of transmitted THz beam at 200 μm going through an envelope with a nut inside.

As a part of the demonstration of our operational THz spectrometer, we have taken a THz image of a hexagon-shaped metallic nut, see Fig. 5. Such an image was taken by mechanically scanning the nut across the THz beam. The transmitted THz beam was then measured by using our bolometer. One can clearly recognize the shape of the hexagon from the THz image. Our THz image has a much higher spatial resolution than those measured using ultrafast THz pulses. In addition, we can gain much more information on the target by using the wavelength of the source as the third dimension. We are currently working on a compact version of such an imaging system.

Observation of up-conversion

In the past, nanosecond THz pulses can only be measured by a bolometer cooled to 2 K. We have implemented a new detection system by utilizing an up-conversion process. We mixed the nanosecond THz pulses in the wavelength range of 92.4-124 μm with an IR beam at 1.064 μm in a GaSe crystal. The up-converted signal near 1.064 μm was then measured by an InGaAs detector. The lowest peak power for the THz wave measured by us was about 2.5 W (an average power of 125 nW). The responsivity for the entire detection system is measured to be 0.10 mV/W. *This result should be regarded as a very important step for us to eventually implement a THz chemical analyzer working at room temperature, to be deployed in the battlefields.*

Investigation of photonic bandgap crystals

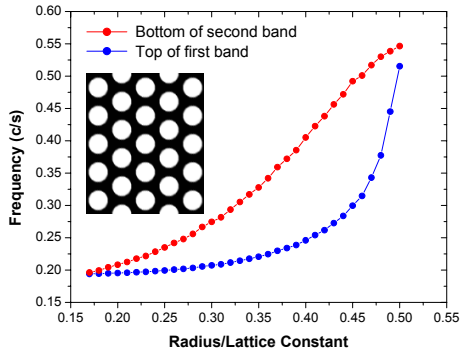

Fig. 6. For a structure of photonic bandgap crystals, formed by drilling circular holes on a Si wafer, the frequencies for the bottom and top of the bandgap are plotted vs. ratio of radius and lattice constant.

We have designed, fabricated, and tested 2-D photonic bandgap crystals. During this period, we have been focusing on a triangular lattice formed by drilling periodic air circles on a Si wafer, see Fig. 6. If one circle is missing, photon defect states can be formed, see Fig. 7. We have used the software from RSoft to design and optimize our photonic bandgap crystal structure. Due to the limitation imposed by the fabrication procedure (i.e. deep reactive ion etching), we have chosen the second bandgap for demonstration, which is formed between band 7 and band 8. Fig. 8(a) illustrates some of the photonic bands for the triangular lattice formed on a Si wafer. In fact, using deep reactive ion etching, the aspect ratio of 10:1 to 15:1 on the fabricated structure can be maintained. This means that for the etched depth of 150 μm, the diameter of the circle at the bottom of the wafer can be larger than that at the top by as much as 20 μm. Therefore, we need to design the structure of the photonic bandgap crystals, which has a relatively large diameter of the circles such that the tapers of the cylindrically-shaped walls would not seriously affect the photonic bandgaps. Furthermore, the width of each bridge connecting the adjacent circles must be wide enough for the structure to survive the fabrication procedure. These are the reasons why we have used the second bandgap instead of the first one in Fig. 8(a). Of course, by making such a choice, we must pay the price. As one can see from Fig. 8(a), the width of the second bandgap is significantly narrower than the half of that for the first bandgap.

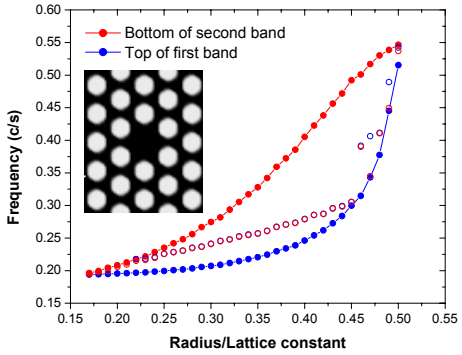

Fig. 7. For photon defect states (open circles), formed by not etching one circular hole in the structure of the photonic bandgap crystals fabricated on a Si wafer, the frequencies for the bottom and top of the bandgap are plotted vs. ratio of radius and lattice constant.

It is important for us to note that for the wafer thickness of 530 μm used in our fabrication and testing experiments, a THz wave must propagate in the photonic-crystal structure as a guided mode, i.e. the THz wave is confined by the air sandwiching the Si wafer just like a slab waveguide. Therefore, the effective index (modal index) instead of the bulk value should be used. In Fig. 8(b), we have plotted the same number of the bands, however, assuming the index is 10% less than the bulk value. For comparison, we have also plotted our calculations on the same number of the bands when the index is 10% larger, see Fig. 8(c). One can see that the bandgap is indeed reduced when the index is reduced. On the other hand, the frequencies existed within the bandgap are increased. When designing the 2-D photonic bandgap structures, we have taken into consideration these factors. Therefore, we have designed the first triangular 2-D photonic bandgap structure. It consists of six columns of the circular holes with the diameter of 120 μm each and the distance of 199 μm between the adjacent ones (center to center). Such a structure was fabricated by us using deep reactive ion etching at Cornell Nanfabrication Facility.

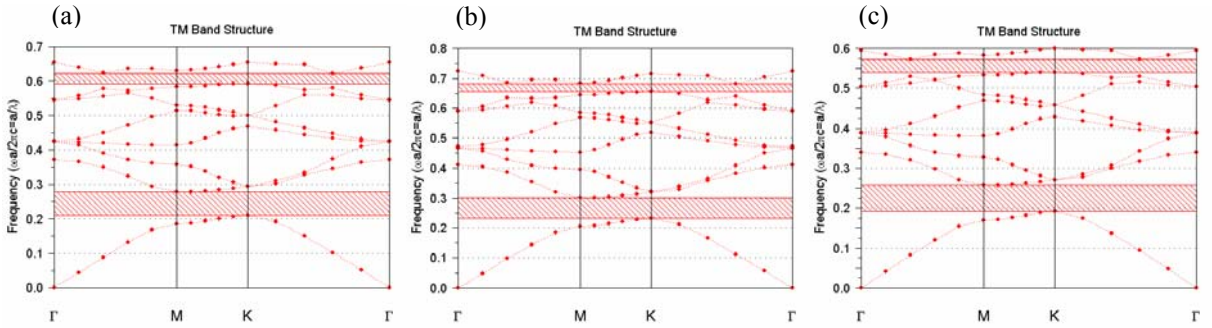

Fig. 8. Dispersion curves for different photonic bands are shown for (a) optimized index of refraction; (b) index is assumed to be 10% less than the value used in (a); and (c) index is assumed to be 10% larger than the value used in (a).

After this structure was fabricated by us, we used our widely-tunable THz source to measure the transmission of the THz beam propagating through the structure. In order to increase the signal-to-noise ratio, we vertically stacked four samples. As a result, the entire THz beam can pass through the photonic-bandgap structure. We have measured and plotted the transmission vs. the incident wavelength for three different incident angles, see Fig. 9. One can see that in the case of the normal incident, it appears that there is a bandgap defining between 300 μm and 450 μm, however, with three small bumps between them. On the other hand, for the incident angles of 10 and 20 degrees, respectively, the bumps near 350 μm become much more pronounced. In addition, the left peak defining the photonic bandgap near 250 μm for the normal incident is significantly blue-shifted when the incident angle is increased to 20 degrees. One can see from Fig. 8(a) that based on our theory the bandgap is formed between 320 μm and 336 μm. Moreover, according to our theory the lower limits defining the bandgaps are blue-shifted as the incident angle increases. Since our theoretical calculations are made by assuming an infinite number of the circles, they are expected to significantly deviate from our experimental results. Nevertheless, we have demonstrated the existence of 2-D photonic bandgaps.

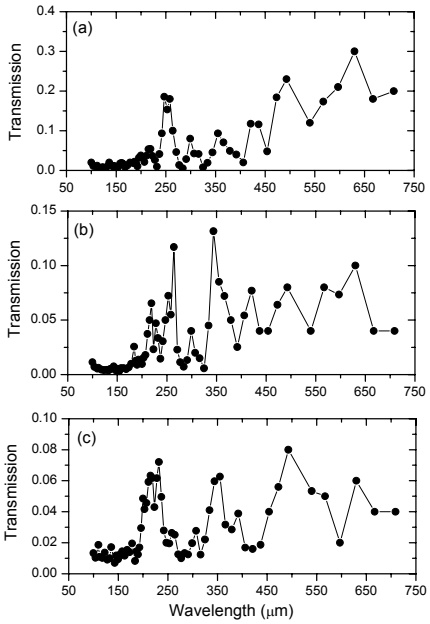

Fig. 9. Transmission vs. incident wavelength for (a) normal incident; (b) incident angle of 10 degrees; and (c) incident angle of 20 degrees.

We have also been focusing on the optimization of PBC's. First of all, we have investigated the dependence of the bandgaps on the fluctuation of the diameters of the circles formed on Si wafers (square and triangular lattices). We start from simple 1-D structures. We assume that the diameters of the circles formed on a Si wafer can be different from one column to the next. In order to gain physical insight, we have compared the bandgaps for three different structures. The first one corresponds to a perfect PBC in which all the circles have exactly the same size. In the second and third ones, however, we assume that every the other column of the circles has a diameter which is 10% smaller or larger. Fig. 10 shows our results based on the calculations made by using the R-Soft software. For the perfect structure, the bandgap is formed between 0.2712 a/λ (a – lattice constant and λ – wavelength) and 0.2986 a/λ. On the other hand, when the

diameter is 10% larger, the bandgap is formed between 0.2853 a/λ and 0.3184 a/λ. When the diameter is reduced by 10%, however, the bandgap is formed between 0.2517 a/λ and 0.2801 a/λ. Therefore, the bandgap is increased by 3.6% and 21% for these two modified structures, respectively. These results are quite encouraging. First of all, the bandgap can be widened by introducing two different sizes of the holes in the PBC. Second, the bandgap becomes even wider if a column of the larger circles is introduced into the PBC's.

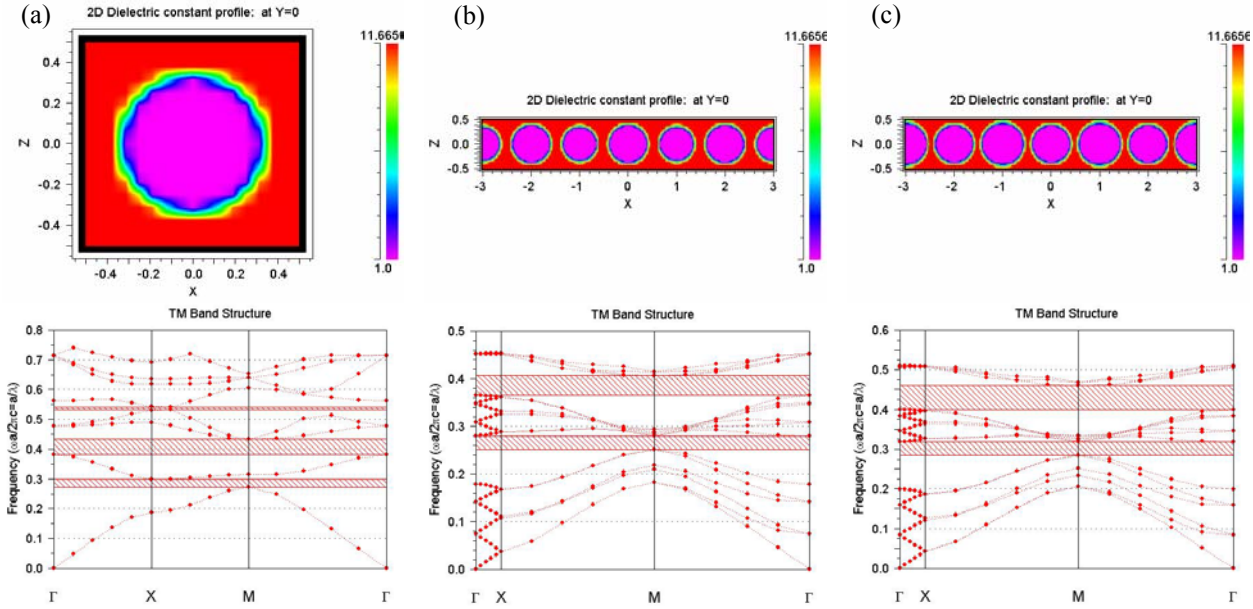

Fig. 10. (a) For square lattice in which all holes have exactly the same diameter, frequency is plotted vs. wave vector. (b) For square lattice in which every the other column of holes is 10% smaller in diameter, frequency vs. wave vector. (c) For square lattice in which every the other column of holes is 10% larger in diameter, frequency vs. wave vector.

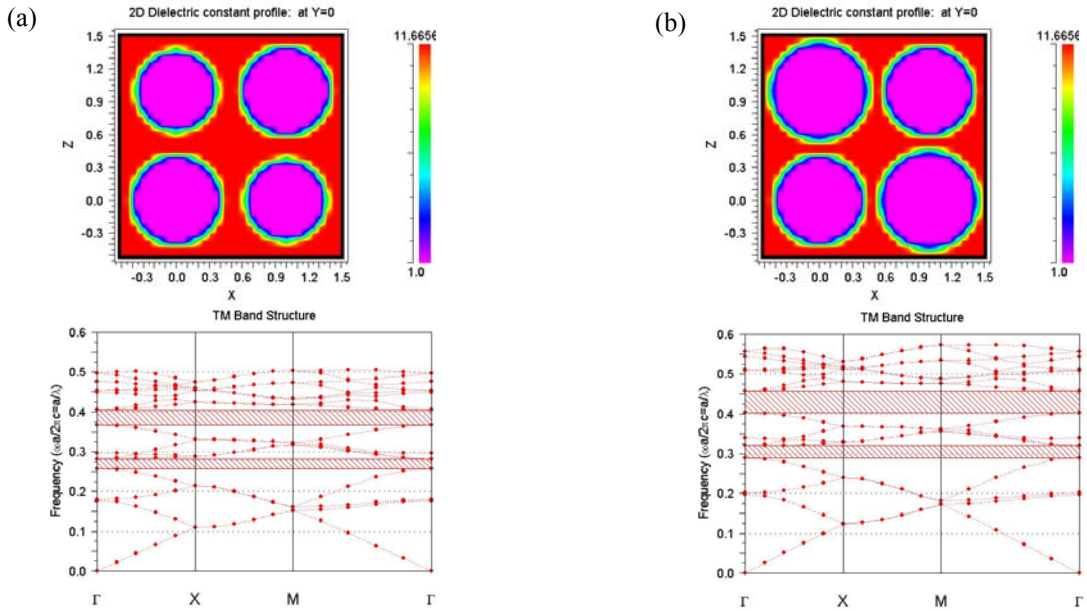

Fig. 11. (a) For 2×2 super cell in square lattice, in which two holes in diagonal are 10% smaller in diameter, frequency is plotted vs. wave vector. (b) For 2×2 super cell in square lattice, in which two holes in diagonal are 10% larger in diameter, frequency is plotted vs. wave vector.

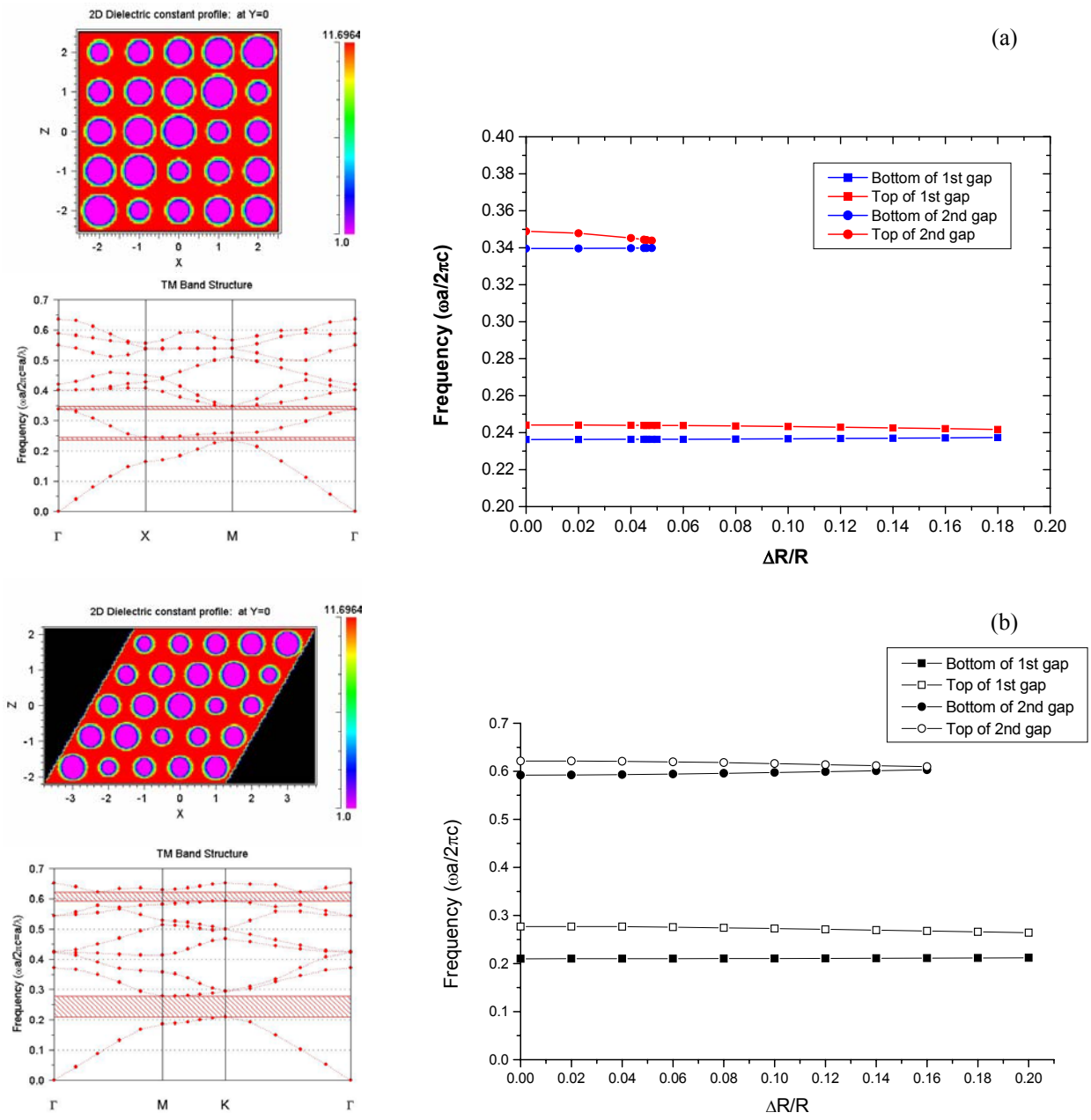

Fig. 12. For super cell consisting of 5×5 holes fabricated on a Si wafer, with diameters semi-randomly distributed: (a) square lattice and (b) triangular lattice, frequency vs. wave vector and frequency vs. maximum fluctuation of radius with respect to average diameter.

After obtaining these results, we have taken one step further by considering 2-D PBC's. In particular, we assume that a super cell consists of 2×2 of the square lattice, in which two holes in the diagonal have the same diameter, but 10% less than the original size of the two holes in the off-diagonal. Another case corresponds to that the diameter for the two holes in the diagonal is 10% larger in size than the two holes in the off-diagonal. Our results are shown in Fig. 11. One can see when the diameter is 10% smaller, the bandgap is formed between 0.2577 a/λ and 0.2811 a/λ (bandgap of 0.0234 a/λ). On the other hand, when the diameter is 10% larger, the

bandgap is formed between 0.2899 a/λ and 0.3197 a/λ (bandgap of 0.0298 a/λ). Compared with the uniform and original diameter of the circles, the bandgap is changed by -14.6% and 8.8%, respectively.

What about the PBC's with randomly-distributed diameter of the circles? It is quite difficult or perhaps impossible to use the R-Soft software to calculate the bandgaps for such a PBC structure. However, we could construct a PBC with semi-randomly-distributed sizes. We have considered square and triangular lattices in which each super cell consists of 5×5 circular holes, see Fig. 12. We then assume that the first row has five different sizes. The second, third, fourth, and fifth rows have the five holes each, which have the same sizes as the first row, but the sequence has been randomly selected. We have calculated the first and second bandgaps, see Fig. 12. One can see that for the square lattice with r/s = 0.34 both the first and second bandgaps are quite narrower. In addition, the first bandgap disappears when the fluctuation is larger than 18% while the second bandgap disappears when the fluctuation is larger than 5%. Therefore, the second bandgap cannot be used in practice since it is nearly impossible to control the fluctuation down to 5% with the current fabrication technology. In comparison, for the triangular lattice with r/s = 0.30 the first bandgap is insensitive to the fluctuation of the radius for the circle. On the other hand, the second bandgap is much narrower and quite sensitive to the radius fluctuation. Furthermore, when the fluctuation is larger than 16% the second bandgap disappears. Based on our results, it is obvious that we should choose the first bandgaps for the square and triangular lattices. However, in reality the situation is quite complicated. Indeed, in order to make sure that the PBC's survive the process of deep reactive ion etching, we must design the PBC structure in such a way that it has sufficiently wide bridges that connect between the adjacent circles. One way to achieve such a goal is to use the second bandgap instead of the first for the triangular lattice. In this case, the lattice constant can be larger. Therefore, the width of the bridges can be wider. While designing the PBC's, we must make sure that the fluctuation is sufficiently low not to destroy the bandgap or to make the bandgap immeasurable. Therefore, our simulation can be extremely important for optimizing the PBC structures.

One Ph.D. student at Lehigh University has spent four weeks at CNF to fabricate the optimized PBC's. The second Ph.D. student has carried out the simulations on PBC's. For the rest of our SBIR project, we will characterize the PBC's just fabricated at CNF and use the R-Soft software to explain and support our experimental results. After that, we will further optimize PBC's following our experimental results, fabricate them at CNF, and then test them at Lehigh University. We believe the results obtained during Phase I can be crucial to the successful completion of our proposed Phase-II work.